Tin-Coated Viral Nanoforests as Sodium-Ion Battery Anodes

Yihang Liu,[†] Yunhua Xu,[†] Yujie Zhu,[†] James N. Culver,[‡] Cynthia A. Lundgren,[§] Kang Xu,[*,§] and Chunsheng Wang[*,†]

[†]Department of Chemical and Biomolecular Engineering, University of Maryland, College Park, Maryland 20742, United States, [‡]Institute for Bioscience and Biotechnology Research and Department of Plant Science and Landscape Architecture, University of Maryland, College Park, Maryland 20742, United States, and [§]Electrochemistry Branch, U.S. Army Research Laboratory, Adelphi, Maryland 20783, United States

ABSTRACT Designed as a high-capacity alloy host for Na-ion chemistry, a forest of Sn nanorods with a unique core—shell structure was synthesized on viral scaffolds, which were genetically engineered to ensure a nearly vertical alignment upon self-assembly onto a metal substrate. The interdigital spaces thus formed between individual rods effectively accommodated the volume expansion and contraction of the alloy upon sodiation/desodiation, while additional carbon-coating engineered over these nanorods further suppressed Sn aggregation during extended electrochemical cycling. Due to the unique nanohierarchy of multiple functional layers, the resultant 3D nanoforest of C/Sn/Ni/TMV1cys, binder-free composite electrode already and evenly assembled on a stainless steel current collector, exhibited supreme capacity utilization and cycling stability toward Na-ion storage and release. An initial capacity of 722 mA·h (g Sn)$^{-1}$ along with 405 mA·h (g Sn)$^{-1}$ retained after 150 deep cycles demonstrates the longest-cycling nano-Sn anode material for Na-ion batteries reported in the literature to date and marks a significant performance improvement for neat Sn material as alloy host for Na-ion chemistry.

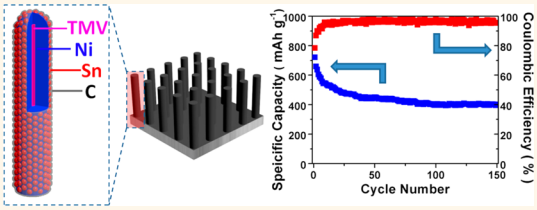

KEYWORDS: Na-ion batteries · Sn nanoforest anodes · nanohierarchy · tobacco mosaic virus · physical vapor deposition · magnetron sputtering

Since their commercialization two decades ago, Li-ion batteries have essentially dominated the portable electronics applications in small formats while being poised to enter more profitable and strategically important markets of automotive and grid storage. However, the limited abundance of Li in the Earth's crust, its uneven geographic distribution and difficulties in recycling Li resources have raised concerns about large scale application of this chemistry. As an alternative to Li-ion chemistry, Na-ion batteries have attracted increasing attention, both because of the low cost associated with its high natural occurrences in both earth and ocean and decent energy densities bestowed by its similar chemical nature to Li. Given this similarity, many mature electrode materials for Li-ion chemistry have been investigated as drop-in replacements for Na-ion; however, most of the efforts were rendered ineffective, as evidenced by the low capacity utilization, inferior rate capability, poor cycling stability, or even complete electrochemical inactivity, for which the larger size of Na-ion relative to Li-ion is generally believed to be responsible.[1,2] More specifically, although a few cathode candidates borrowed from Li-ion chemistry do intercalate/deintercalate Na-ion reversibly,[3−18] the availability of such anode materials is much more rare. It has been reported that carbonaceous materials,[19−23] TiO_2,[24] Sb_2O_4,[25] Sb,[26] SnSb,[27] and Sn[28−30] can store and release Na-ion with decent reversibility, among which an Sb/C composite seems to provide the best performance of 575 mA·h g^{-1} over 100 cycles.[26] Despite the high theoretical capacity of Sn (847 mA·h g^{-1} corresponding to $Na_{15}Sn_4$), the much larger volume expansion of Sn (520%) than Sb (390%) during sodiation essentially prevents the access of this capacity.[27,29] This effect of volume change has been familiar for Si or Sn as lithiation hosts, and the larger size of Na-ion significantly worsened it. In addition to this complication, Sn particles also tend to aggregate into large particles and then pulverize to isolate from electrode during electrochemical alloying/dealloying, which further disrupts the electrode integrity and leads to rapid deterioration in cycling stability.[31] Mainly because of these two failure

* Address correspondence to conrad.k.xu.civ@mail.mil, cswang@umd.edu.

Received for review February 4, 2013 and accepted March 13, 2013.

Published online March 13, 2013
10.1021/nn400601y

© 2013 American Chemical Society

mechanisms, the best cycle life reported for nano-Sn was represented by less than 25 charge/discharge cycles for Na-ion storage.[28,30] To circumvent these issues, Xiao *et al*. developed nanosized binary elemental alloys such as SnSb/C to reduce stress/strain and to dilute the opportunities for Sn aggregation, which achieved an unprecedented capacity of 435 mA·h g^{-1} over 50 cycles.[27]

In this work, we adopted two separate strategies to address the issues of pulverization and aggregation of Sn-based anodes. First, we introduced nanohierarchy into Sn electrodes by depositing Sn nanoparticles on Ni-coated tobacco mosaic virus (TMV), which was genetically modified to express 100% cysteine on its major coat protein. Viruses have been successfully used as a bioinorganic template to synthesize electrode materials for rechargeable batteries,[32] and TMV1cys has been demonstrated to be a versatile template for 3D nanoforest electrodes of a number of different chemistries.[33] Taking advantage of the well-understood 3D structure of TMV, a novel mutant TMV1cys was created *via* genetic engineering, wherein a cysteine codon is expressed within the N-terminus of coat proteins.[34−36] The thiol group in cysteine is known to interact with metal surfaces; however, in TMV1cys most cysteines are partially recessed in a groove covered by the C-terminal arm of the coat protein and are thus incapable of metal binding. The only exception occurs at the 3′-end of the nanorods, where cysteines are well exposed and available for metal binding. This peculiar configuration leads to the near-vertical assembly of these nanorods onto a metal surface (Figure 1).

After Sn nanoparticles were deposited over the Ni interlayer formed by electroless plating, the buffering spaces between each individual nanorod would effectively accommodate the volume expansion of Sn while still maintaining high capacity loading per footprint. Second, a thin layer of carbon was coated over the active Sn sublayer, suppressing possible aggregation during the electrochemical reactions by diminishing the diffusion of Sn (Figure 1).

With this hierarchy consisting of multiple functional layers on nanoscale, we anticipated that the stress caused by the large volume change of Sn would be effectively alleviated[37,38] and a highly conductive pathway for electrons would be established by the Ni sublayer between the Sn and current collector. It was also known that Ni nanorods can alloy with Sn, which would enhance the robustness of Sn particles through intermetallic bonding potentially.[39−45] Additional coating of a carbon sublayer over the Sn should suppress aggregation and pulverization of Sn, further improving electrochemical performance.[46−50]

Thus, the Sn nanoforest anode was fabricated on the Ni/TMV1cys assemblies that are vertically aligned on a stainless steel (SS) current collector. A ~50 nm nickel coating was first deposited on TMV1cys nanorods in an electroless plating bath to form a longitudinal electron pathway along the inner core of each nanorod (Figure 2a,b). A rough layer (20 nm) of Sn (Figure 2c) and a 5 nm layer of carbon (Figure 2d) were then sequentially placed onto the Ni sublayer using physical vapor deposition (PVD) and radio frequency (RF) magnetron sputtering deposition, leading to the configuration of C/Sn/Ni/TMV1cys.

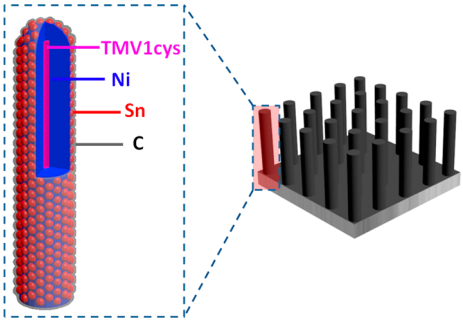

Figure 1. Schematic illustration of the 3D C/Sn/Ni/TMV1cys anode arrays and the cross-section of hierarchical structure of a single Sn nanorod.

RESULTS AND DISCUSSION

Figure S1, Supporting Information, and Figure 3a,b show the SEM images of near-vertical assembly of Ni/TMV, Sn/Ni/TMV, and C/Sn/Ni/TMV on a SS current collector, respectively. As a reference for comparison, a 2D Sn thin film with 20 nm thickness was also directly deposited on the SS substrate under the same conditions (Figure S2a, Supporting Information). The hierarchy, structure, and configuration of virus-templated C/Sn nanorods were further confirmed by transmission electron microscopy (TEM) and energy-dispersive spectroscopy (EDS). Figure 3c−f show the TEM images of single Sn/Ni/TMV1cys and C/Sn/Ni/TMV1cys nanorods and the EDS line scan mapping profile with the high-resolution images. In Figure 3c, a thin layer of Sn was clearly visible with thickness of ~20 nm, whose loading is ~0.5 mg cm^{-2} in mass. The loading mass of Sn was obtained by weighing the mass difference before and after Sn physical vapor deposition using a high-precision microbalance (Mettler Toledo, XS105 dualRange) within an accuracy of 1 μg. The EDS line scan mapping demonstrated the layer structure and confirmed the SEM images shown in Figure 3b. Both SEM and TEM images cooperatively revealed that all the nanorods have a Ni/TMV1cys core that is directly mounted on the SS main current collector, providing a longitudinal current collector sublayer. This metallic nanotube has been proven effective in resolving issues associated with electron-transfer kinetics along the high aspect-ratio nanorod- or nanowire-like materials, for which nanoscale intimacy between all functional sublayers has been a challenge.[33]

It should be noted that after carbon coating, the Sn-sublayer structure anchored on the Ni nanoshell

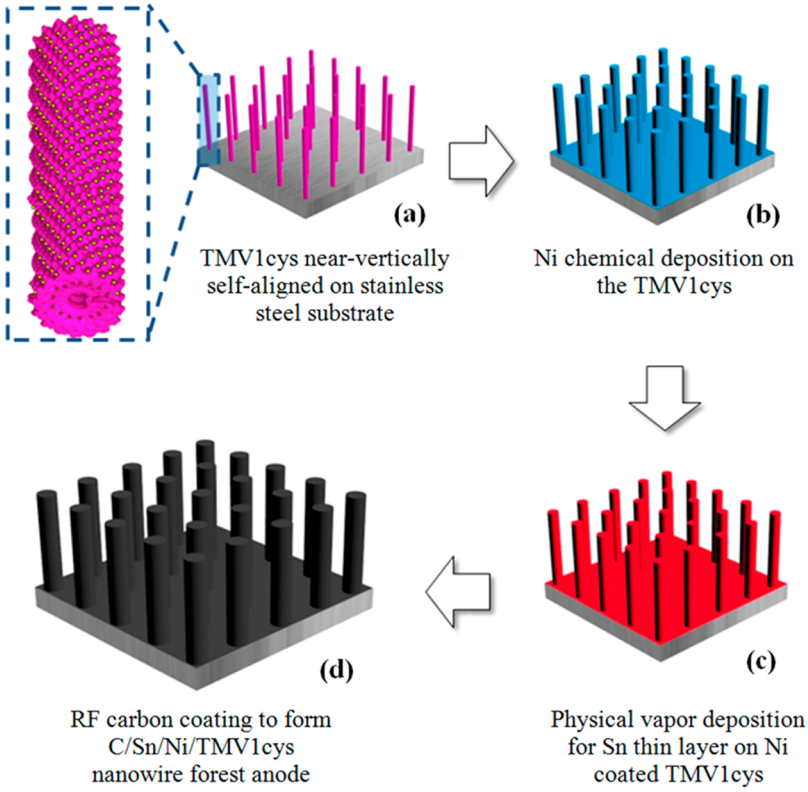

Figure 2. Schematic illustration of nanohierarchical 3D anode arrays consisting of TMV1cys/Ni/Sn/C self-aligned on stainless steel.

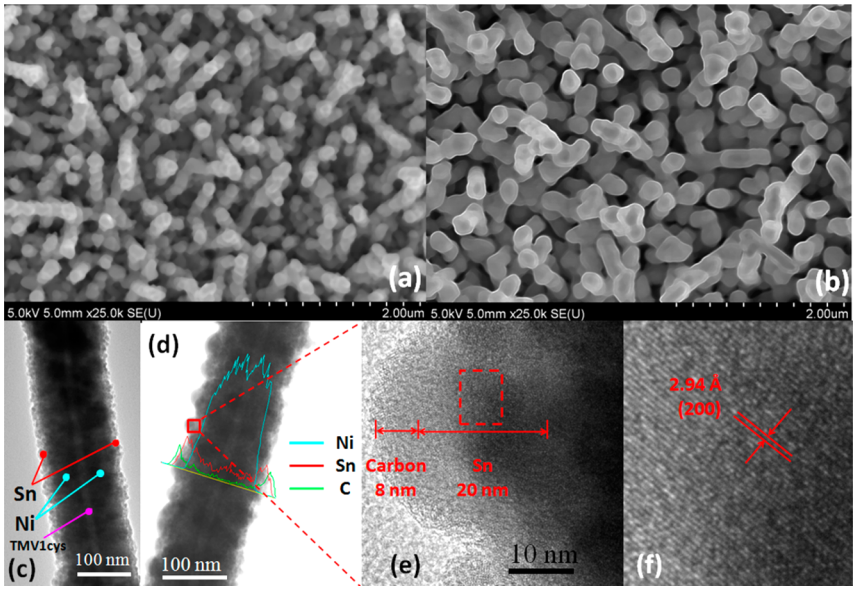

Figure 3. SEM images of as-deposited (a) 3D Sn/Ni/TMV1cys and (b) 3D C/Sn/Ni/TMV1cys anodes. (c) TEM image of a single C/Sn/Ni/TMV1cys nanorod and (d) its EDS line scan mapping profile, (e) high-resolution TEM image of the Sn crystal and the amorphous outer layer, and (f) enlarged high-resolution TEM image of the Sn crystal of the red rectangle area in panel e.

changed from smooth thin film (Figure 3c) to a more particulated shape (Figure 3d), indicating that the Sn thin layer may have aggregated into nanoparticles during the RF carbon sputtering deposition process. The high-resolution TEM image (Figure 3e,f) shows a core−shell configuration for these C/Sn particles with a crystalline core and an amorphous shell layer; a 2.94 Å interplanar space can be assigned to the (200) plane of Sn in Figure 3f. From the EDS line scan mapping in Figure 3d and TEM in Figure 3e, the thickness of carbon layer on the surface of the Ni nanorods is ~5 nm. The graphitization degree of the carbon layer was

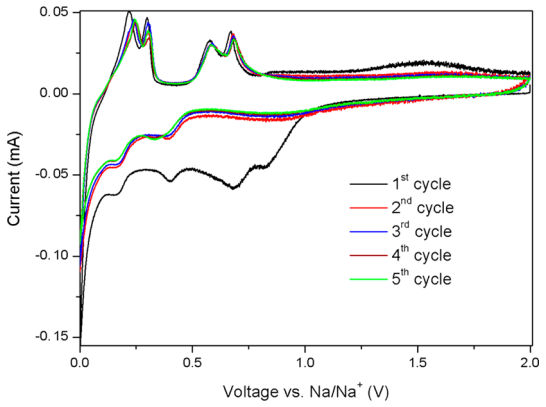

Figure 4. Cyclic voltammetry of C/Sn/Ni/TMV1cys nanoforest anode with a scan rate of 0.1 mV s^{-1} between 0.0 and 2.0 V.

investigated using the Raman spectrum (Figure S3, Supporting Information), showing two bands of D and G at 1371 and 1542 cm^{-1}, respectively, in accordance with disorder and graphitic crystal features of carbon.[51] The stronger D band suggests that the carbon layer on the C/Sn/Ni/TMV1cys nanorods has low crystallinity, typical of disordered carbonaceous material.

Summarizing the images and chemical analyses, the composite electrode array templated on virus carries nearly uniform Sn active sublayers in a multilayered nanohierarchy, wherein primary Sn nanoparticles reside on a secondary nanorod vertically standing on current collector, while additional inert ingredients exist between active materials and current collector as functional sublayers. The overall electrochemical performance should be improved due to the array's spatial tolerance against accommodating volume change, its mechanical robustness to maintain material integrity, its high electron conductivity in the longitudinal direction, and its 3D architecture to store Na-ions vertically above the main current collector.

The electrochemical performance was investigated in coin cells using Na metal as the counter electrode, and 1 M $NaClO_4$ in ethylene carbonate/diethyl carbonate (EC/DEC, 1:1 by vol %) as electrolyte. All electrochemical experiments were conducted at room temperature, and all capacities were calculated based on the weight of Sn. The sodiation and desodiation of C/Sn/Ni/TMV nanoforest anodes was characterized using cyclic voltammetry (CV). As shown in Figure 4, five peaks, located at 0.82, 0.68, 0.40, 0.15, and 0.0 V, were observed in the first sodiation process. Because the two sodiation peaks at higher voltage disappeared in the subsequent cycles, they were possibly attributed to the formation of solid electrolyte interphase (SEI) film caused by the decomposition of electrolyte, which contributes to the irreversible capacity. The desodiation process presents four well-defined peaks at 0.22, 0.30, 0.58, and 0.67 V, which are attributed to the alloy compounds of $Na_{15}Sn_4$, Na_9Sn_4, NaSn, $NaSn_5$, respectively, with a two-phase reaction mechanism.[29] All these desodiation potentials are in good agreement with the calculated and experimental results of Sn reported previously.[27−30] The Ni (or potentiall NiO) core in C/Sn/Ni/TMV anodes turned out to be inactive for Na.[25] The contribution in capacity from carbon coating can be neglected due to the low presence of carbon in the composite material (C/Sn = 7 wt %). The unchanged peak current intensity implies excellent reversibility of the C/Sn/Ni/TMV1cys nanoforest anode.

The cycling performance of 3D Sn/Ni/TMV1cys and 3D C/Sn/Ni/TMV1cys anodes was investigated by galvanostatic charge and discharge of the electrodes between 0.05 and 1.5 V at the current density of 50 mA g^{-1} (Figure 5a), with 2D Sn thin film (with the same thickness of 20 nm as 3D nanoforest Sn anode) as reference for comparison. All three Sn anodes provided around 730 mA·h g^{-1} at the first desodiation process, which is close to the theoretical capacity (847 mA·h g^{-1}) corresponding to $Na_{15}Sn_4$, approximately three times larger than that of hard carbon. The 2D Sn thin film anode suffered a rapid capacity fading, retaining only 9% of the initial capacity within 5 cycles. In contrast, the Sn/Ni/TMV1cys nanoforest anode maintains 30% of initial capacity after 20 cycles, which is a visible improvement over that of reference. After 40 cycles, its capacity stabilized at ~100 mA·h g^{-1}. The cycling stability was significantly extended by a thin layer (5 nm) carbon coating on the Sn/Ni/TMV1cys nanoforest: after a slight decrease in the initial few cycles, the capacity stabilized around 405 mA·h g^{-1} after 150 cycles, corresponding to retention of 55%, which is much higher than those without carbon coating, demonstrating that carbon coating can effectively suppress Sn aggregation.

Aside from capacity, voltage profiles actually reveal more details about the electrochemistry of sodiation/desodiation in a Sn host. These voltage profiles of 2D Sn thin film, 3D Sn/Ni/TMV1cys, and 3D C/Sn/Ni/TMV1cys anodes are depicted in Figure 5b−d, respectively, with cycle numbers labeled on individual curves. The step potential plateaus between 0.0 and 0.7 V were presented in the first desodiation for all three kinds of anodes, which is characteristic of dealloying $Na_{15}Sn_4$. This is consistent with the CV curves in Figure 4. As shown in Figure 5b, the capacity in each potential plateau of the 2D Sn thin film anodes rapidly decreased with cycling, suggesting that the Sn film disintegrated and detached electronically from the current collector. In contrast, the step potential plateaus of 3D Sn/Ni/TMV1cys anodes remained visible even after 10 cycles, but eventually disappeared after 150 cycles (Figure 5c), indicating that the nanostructure of Sn/Ni/TMV helped but was still not robust enough to withstand the volume change and aggregation in extended charge/discharge cycles. However, the thin layer carbon coating made a much more pronounced difference,

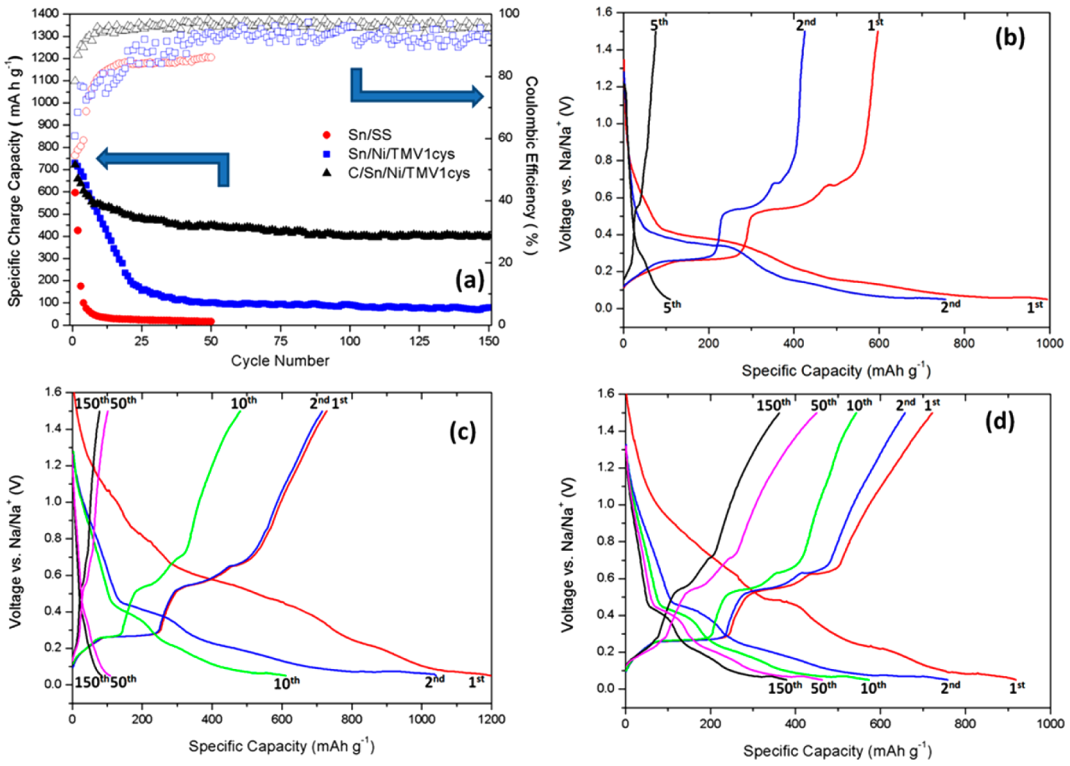

Figure 5. (a) Cycling performance of 2D Sn thin film, 3D Sn/Ni/TMV1cys, and 3D C/Sn/Ni/TMV1cys anodes and sodiation/desodiation voltage profiles of (b) 2D Sn thin film, (c) 3D Sn/Ni/TMV1cys, and (d) 3D C/Sn/Ni/TMV1cys nanoforest anodes at current density of 50 mA g^{-1}.

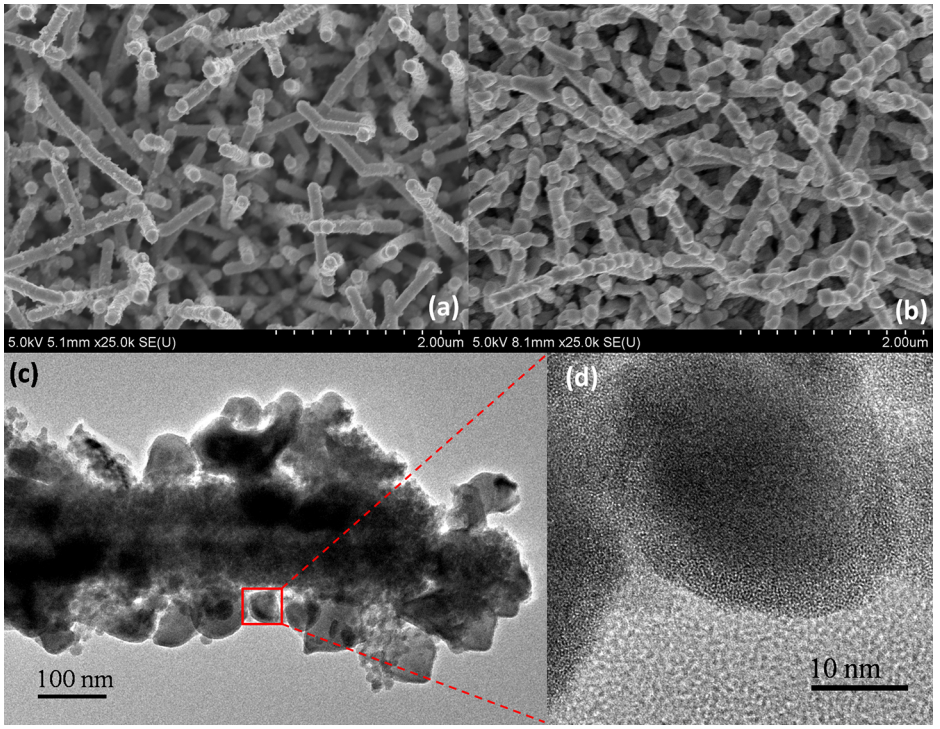

Figure 6. SEM images of (a) 3D Sn/Ni/TMV1cys anode and (b) 3D C/Sn/Ni/TMV1cys anode after 150 charge/discharge cycles at current density of 50 mA g^{-1}; (c) TEM image of a single C/Sn/Ni/TMV1cys nanorod after 150 charge/discharge cycles at current density of 50 mA g^{-1} and (d) enlarged high-resolution TEM image of the after-cycling amorphous Sn.

maintaining these distinct step plateaus even after 150 full charge/discharge cycles (Figure 5d).

To gain insight into the capacity fading mechanism and any accompanying structural change of these

anodes during cycling, SEM and TEM images were collected from 2D Sn thin film anode after 50 cycles, 3D Sn/Ni/TMV1cys and 3D C/Sn/Ni/TMV1cys anodes after 150 cycles, respectively, as shown in Figure S2b and Figure 6. Sn nanoparticles in 2D thin film apparently coalesced into large particles and pulverized as demonstrated in Figure S2b, and most Sn peeled off from the current collector, leading to severe capacity fading. In 3D Sn/Ni/TMV1cys anodes, although some Sn still remained on the Ni/TMV1cys nanorods after 150 cycles (Figure 6a) thanks to the nanostructure, the cleaner surfaces of Sn/Ni/TMV nanorodes suggested that the majority of Sn particles detached from the Ni nanorod current collectors. The reason is probably the same as the 2D Sn thin film anode where the Sn particles tend to aggregate to larger particles during sodiation/desodiation processes, a process likely driven by the thermodynamics of intermetallic alloy compounds. Once the Sn particles grew to certain size, they pulverized and lost contact with current collectors, thus becoming electrochemically inactive.

On the other hand, the after-cycling SEM image of C/Sn/Ni/TMV1cys (Figure 6b) clearly shows that the most of the Sn sublayer still remained on the nanocurrent collectors even after 150 cycles, and the growth of Sn particle size is apparently suppressed (Figure 6c), most likely due to the protection effects of the carbon coating. This validates our hypothesis that Sn aggregation during electrochemical extended sodiation/desodiation cycles could be mitigated by carbon coating, based on earlier experience that carbon has been effective in suppressing Sn aggregation during lithiation/delithiation.[46−50]

The crystal-to-amorphous transit of Sn in C/Sn/Ni/TMV1cys anodes is also observed in the after-cycling TEM images (Figure 6d). Some Sn became amorphous after 150 sodiation/desodiation cycles. In addition to the loss of active Sn material due to electrode disintegration, this crystal-to-amorphous transition constitutes another reason for the disappearance of plateaus in Figure 5b−d. The C/Sn/Ni/TMV1cys sample obtains the best stability among the three electrodes, not only because of the 3D nanostructure enabled by viral templates but also because the carbon coating physically separates the crystal particles and prevents the aggregation among the Sn particles. The total mass loading of Sn on the 3D Ni/TMV1cys nanoforest is ~0.5 mg cm^{-2}, corresponding to a footprint capacity of 0.2 mA·h cm^{-2} for Na-ion batteries. The capacity of the 3D Sn/Ni/TMV1cys nanoforest anodes for Na-ion batteries is comparable with the 3D Fe_3O_4 anodes,[52] 3D $LiCoO_2$ cathodes,[53] and TiO_2 anodes[54] for Li-ion batteries. Considering that the electrodes in Na-ion batteries normally have lower capacity than in Li-ion batteries, we believe that the capacity per footprint achieved in this work represents a breakthrough with promising practical perspectives.

CONCLUSIONS

In summary, 3D Sn nanoforest anode arrays consisting of individual nanorods, whose multiple functional layers include a carbon outer shell, a Sn intermediate layer and a metal inner core, were fabricated by PVD, RF magnetron sputtering, and electroless deposition on patterned TMV1cys templates. The C/Sn/Ni/TMV1cys nanorods with ~20 nm thickness of Sn demonstrated superior electrochemical performance toward Na-ion storage and release. The vertical alignment of nanorods as well as the precise hierarchical control of various sublayers of materials in designed order were believed to function synergistically to maintain an alloy anode host mechanically, electronically, and electrochemically stable, despite its >500% volume change upon sodiation/desodiation cycles. In particular, the carbon coating on the Sn particles minimized the Sn particle aggregation, which has been a rather severe challenge that this high-capacity alloy host is facing. The resultant C/Sn/Ni/TMV1cys nanorods can provide 722 mA·h g^{-1} capacity toward Na-ion in the initial cycles and retain 405 mA·h g^{-1} after 150 cycles, demonstrating the longest-cycling nano-Sn anode material for Na-ion batteries reported in the literature to date. The superior cycling performance, combined with the simplicity of the TMV1cys self-assembly and patterning process, represents a new strategy for the development of inexpensive and versatile synthesis techniques for Na-based energy-storage applications.

EXPERIMENTAL METHODS

Sn Anode Fabrication. The Sn layer was deposited on stainless steel (SS) discs (14.25 mm in diameter) containing preassembled Ni-coated TMV1cys templates by physical vapor deposition (PVD) under continuous vacuum. The SS discs were polished carefully and cleaned by sonication in alcohol and acetone before loading into the vacuum chamber. The synthesis process of 3D TMV1cys templates began with the TMV1cys self-assembly; the polished SS discs were immersed into 0.1 g/L TMV1cys solution with 0.1 M sodium phosphate buffer for 48 h, and then the discs were moved to palladium catalytic solution (Na_2PdCl_4) to activate the cysteine residues on the surface of the TMV1cys. Ni was deposited on the virus by an electroless plating in 0.1 M $NiCl_2$ and 0.5 M $(CH_3)_2NHBH_3$ (dimethylamineborane, DMAB) as a reducing agent. The as-deposited 3D TMV1cys templates were washed with distilled water and dried in a vacuum oven at 100 °C overnight. A Sn pellet (99.999%, Kurt J. Lesker Company) was used as the Sn source for PVD. In order to get a uniform morphology, the Sn deposition rate was kept as low as 0.02 nm s^{-1}. The carbon sputtering was conducted in an Ar atmosphere (1 Pa) using a DC power density of 4.5 W/cm^2. The target-to-substrate separation was 11 cm. In comparison, the Sn/SS thin film anode with a 20 nm thickness was also prepared under the same PVD conditions, and the thickness

was confirmed by the film thickness monitor of the Metra Thermal Evaporator.

Characterization of Sn Nanowire Forest Anodes. The Sn loading mass of each sample was measured with a high-precision microbalance (Mettler Toledo, XS105 dualRange) within an accuracy of 1 μg. Raman scattering spectra were collected with Horiba JobinYvonLabRAM Raman microscopes (model ARAMIS) with a 633 nm excitation line. The surface morphology of the samples was characterized by scanning electron microscopy (HITACHI SU-70). A high-resolution transmission electron microscopy (HRTEM, JEOL JEM 2100F) with an energy-dispersive spectrometer (EDS) was employed to analyze the microstructures and interface characteristics of the film stacks.

Electrochemical Performance Testing. Electrochemical performance of the Sn anodes were tested in coin cells (R2032) using sodium metal as counter electrode and 1 M $NaClO_4$ solution in ethylene carbonate/diethyl carbonate (EC/DEC, 1:1 by vol. %) as electrolyte. The charge/discharge testing was carried out using an Arbin BT-2000 battery test station over the voltage range of 0.05−1.5 V versus Na/Na^+. The cyclic voltammetry (CV) curves were collected using a Solartron 1260/1287 with a scan rate of 0.1 mV s^{-1} and a scan range from 0 to 2 V for 5 cycles. All electrochemical experiments were conducted at room temperature, and all capacity values were calculated based on the weight of Sn.

Conflict of Interest: The authors declare no competing financial interest.

Supporting Information Available: Experimental details, electrochemical tests details, SEM images of 3D Ni/TMV1cys template, as-deposited 2D Sn thin film anode and 2D thin film anode after cycling, and Raman spectra. This material is available free of charge *via* the Internet at http://pubs.acs.org.

Acknowledgment. The authors acknowledge financial support from the U.S. Army Research Laboratory and the technical support of the Maryland NanoCenter. We thank Dr. Li-Chung Lai for the TEM imaging, John Abrahams for the deposition, and Yanmei Piao for collecting the Raman data. Y. Liu was partially supported as part of the Nanostructures for Electrical Energy Storage, an Energy Frontier Research Center funded by the U.S. Department of Energy, Office of Science, Office of Basic Energy Sciences under Award Number DESC0001160.

REFERENCES AND NOTES

1. Palomares, V.; Serras, P.; Villaluenga, I.; Hueso, K. B.; Carretero-Gonzalez, J.; Rojo, T. Na-Ion Batteries, Recent Advances and Present Challenges To Become Low Cost Energy Storage Systems. *Energy Environ. Sci.* **2012**, *5*, 5884–5901.
2. Ong, S. P.; Chevrier, V. L.; Hautier, G.; Jain, A.; Moore, C.; Kim, S.; Ma, X.; Ceder, G. Voltage, Stability and Diffusion Barrier Differences between Sodium-Ion and Lithium-Ion Intercalation Materials. *Energy Environ. Sci.* **2011**, *4*, 3680–3681.
3. Kim, S.-W.; Seo, D.-H.; Kim, H.; Park, K.-Y.; Kang, K. A Comparative Study on Na_2MnPO_4F and Li_2MnPO_4F for Rechargeable Battery Cathodes. *Phys. Chem. Chem. Phys.* **2012**, *14*, 3299–3303.
4. Kim, D.; Lee, E.; Slater, M.; Lu, W.; Rood, S.; Johnson, C. S. Layered $Na[Ni_{1/3}Fe_{1/3}Mn_{1/3}]O_2$ Cathodes for Na-Ion Battery Application. *Electrochem. Commun.* **2012**, *18*, 66–69.
5. Ellis, B. L.; Makahnouk, W. R. M.; Makimura, Y.; Toghill, K.; Nazar, L. F. A Multifunctional 3.5 V Iron-Based Phosphate Cathode for Rechargeable Batteries. *Nat. Mater.* **2007**, *6*, 749–753.
6. Jian, Z.; Zhao, L.; Pan, H.; Hu., Y.-S.; Li, H.; Chen, W.; Chen, L. Carbon Coated $Na_3V_2(PO_4)_3$ as Novel Electrode Material for Sodium Ion Batteries. *Electrochem. Commun.* **2012**, *14*, 86–89.
7. Cao, Y.; Xiao, L.; Wang, W.; Choi, D.; Nie, Z.; Yu, J.; Saraf, L. V.; Yang, Z.; Liu, J. Reversible Sodium Ion Insertion in Single Crystalline Manganese Oxide Nanowires with Long Cycle Life. *Adv. Mater.* **2011**, *23*, 3155–3160.
8. D'Arienzo, M.; Ruffo, R.; Scotti, R.; Morazzoni, F.; Mari, C. M.; Polizzib, S. Layered $Na_{0.71}CoO_2$: A Powerful Candidate for Viable and High Performance Na-Batteries. *Phys. Chem. Chem. Phys.* **2012**, *14*, 5945–5952.
9. Kitajoua, A.; Komatsub, H.; Chiharac, K.; Gochevac, I. D.; Okadac, S.; Yamaki, J. Novel Synthesis and Electrochemical Properties of Perovskite-Type $NaFeF_3$ for A Sodium-Ion Battery. *J. Power Sources* **2012**, *198*, 389–392.
10. Lee, K. T.; Ramesh, T. N.; Nan, F.; Botton, G.; Nazar, L. F. Topochemical Synthesis of Sodium Metal Phosphate Olivines for Sodium-Ion Batteries. *Chem. Mater.* **2011**, *23*, 3593–3600.
11. Reynauda, M.; Barpandaa, P.; Roussec, G.; Chotarda, J.; Melota, B. C.; Rechama, N.; Tarascon, J.-M. Synthesis and Crystal Chemistry of the $NaMSO_4F$ Family. *Solid State Sci.* **2012**, *14*, 15–20.
12. Sathiya, M.; Hemalatha, K.; Ramesha, K.; Tarascon, J.-M.; Prakash, A. S. Synthesis, Structure, and Electrochemical Properties of the Layered Sodium Insertion Cathode Material: $NaNi_{1/3}Mn_{1/3}Co_{1/3}O_2$. *Chem. Mater.* **2012**, *24*, 1846–1853.
13. Yabuuchi, N.; Kajiyama, M.; Iwatate, J.; Nishikawa, H.; Hitomi, S.; Okuyama, R.; Usui, R.; Yamada, Y.; Komaba, S. P2-Type $Na_x[Fe_{1/2}Mn_{1/2}]_2$ Made from Earth-Abundant Elements for Rechargeable Na Batteries. *Nat. Mater.* **2012**, *11*, 512–517.
14. Hamani, D.; Ati, M.; Tarascon, J.-M.; Rozier, P. Na_xVO_2 as Possible Electrode for Na-Ion Batteries. *Electrochem. Commun.* **2011**, *13*, 938–941.
15. Wessells, C. D.; Peddada, S. V.; Huggins, R. A.; Cui, Y. Nickel Hexacyanoferrate Nanoparticle Electrodes for Aqueous Sodium and Potassium Ion Batteries. *Nano Lett.* **2011**, *11*, 5421–5425.
16. Lu, Y.; Wang, L.; Cheng, J.; Goodenough, J. B. Prussian Blue: A New Framework of Electrode Materials for Sodium Batteries. *Chem. Commun.* **2012**, *48*, 6544–6546.
17. Abouimrane, A.; Dambournet, D.; Chapman, K. W.; Chupas, P. J.; Weng, W.; Amine, K. A New Class of Lithium and Sodium Rechargeable Batteries Based on Selenium and Selenium-Sulfur as a Positive Electrode. *J. Am. Chem. Soc.* **2012**, *134*, 4505–4508.
18. Tepavcevic, S.; Xiong, H.; Stamenkovic, V. R.; Zuo, X.; Balasubramanian, M.; Prakapenka, V. B; Johnson, C. S.; Rajh, T. Nanostructured Bilayered Vanadium Oxide Electrodes for Rechargeable Sodium-Ion Batteries. *ACS Nano* **2012**, *6*, 530–538.
19. Alcantara, R.; Jimenez-Mateos, J. M.; Lavela, P.; Tirado, J. L. Carbon Black: A Promising Electrode Material for Sodium-Ion Batteries. *Electrochem. Commun.* **2001**, *3*, 639–642.
20. Komaba, S.; Murata, W.; Ishikawa, T.; Yabuuchi, N.; Ozeki, T.; Nakayama, T.; Ogata, A.; Gotoh, K.; Fujiwara, K. Electrochemical Na Insertion and Solid Electrolyte Interphase for Hard-Carbon Electrodes and Application to Na-Ion Batteries. *Adv. Funct. Mater.* **2011**, *21*, 3859–3867.
21. Wenzel, S.; Hara, T.; Janek, J.; Adelhelm, P. Room-Temperature Sodium-Ion Batteries: Improving the Rate Capability of Carbon Anode Materials by Templating Strategies. *Energy Environ. Sci.* **2011**, *4*, 3342.
22. Komaba, S.; Ishikawa, T.; Yabuuchi, N.; Murata, W.; Ito, A.; Ohsawa, Y. Fluorinated Ethylene Carbonate as Electrolyte Additive for Rechargeable Na Batteries. *ACS Appl. Mater. Interfaces* **2011**, *3*, 4165–4168.
23. Cao, Y.; Xiao, L.; Sushko, M. L.; Wang, W.; Schwenzer, B.; Xiao, J.; Nie, Z.; Saraf, L. V.; Yang, Z.; Liu, J. Sodium Ion Insertion in Hollow Carbon Nanowires for Battery Applications. *Nano Lett.* **2012**, *12*, 3783–3787.
24. Xiong, H.; Slater, M. D.; Balasubramanian, M.; Johnson, C. S.; Rajh, T. Amorphous TiO_2 Nanotube Anode for Rechargeable Sodium Ion Batteries. *J. Phys. Chem. Lett.* **2011**, *2*, 2560–2565.
25. Sun, Q.; Ren, Q.; Li, H.; Fu, Z. High Capacity Sb_2O_4 Thin Film Electrodes for Rechargeable Sodium Battery. *Electrochem. Commun.* **2011**, *13*, 1462–1464.
26. Qian, J.; Chen, Y.; Wu, L.; Cao, Y.; Ai, X.; Yang, H. High Capacity Na-Storage and Superior Cyclability of Nanocomposite Sb/C Anode for Na-Ion Batteries. *Chem. Commun.* **2012**, *48*, 7070–7072.

27. Xiao, L.; Cao, Y.; Xiao, J.; Wang, W.; Kovarik, L.; Nie, Z.; Liu, J. High Capacity, Reversible Alloying Reactions in SnSb/C Nanocomposites for Na-Ion Battery Applications. *Chem. Commun.* **2012**, *48*, 3321–3323.
28. Komaba, S.; Matsuura, Y.; Ishikawa, T.; Yabuuchi, N.; Murata, W.; Kuze, S. Redox Reaction of Sn-Polyacrylate Electrodes in Aprotic Na Cell. *Electrochem. Commun.* **2012**, *21*, 65–68.
29. Chevrier, V. L.; Ceder, G. Challenges for Na-ion Negative Electrodes. *J. Electrochem. Soc.* **2011**, *158*, A1011–A1014.
30. Xu, Y.; Zhu, Y.; Liu, Y.; Wang, C. Electrochemical Performance of Porous Carbon/Tin Composite Anodes for Sodium-Ion and Lithium-Ion Batteries. *Adv. Energy Mater.* **2013**, *3*, 128–133.
31. Winter, M.; Besenhard, J. O. Electrochemical Lithiation of Tin and Tin-Based Intermetallics and Composites. *Electrochim. Acta* **1999**, *45*, 31–50.
32. Lee, Y. J.; Yi, H.; Kim, W.; Kang, K.; Yun, D. S.; Strano, M. S.; Ceder, G.; Belcher, A. M. Fabricating Genetically Engineered High-Power Lithium-Ion Batteries Using Multiple Virus Genes. *Science* **2009**, *324*, 1051–1055.
33. Liu, Y.; Zhang, W.; Zhu, Y.; Luo, Y.; Xu, Y.; Brown, A.; Culver, J. N.; Lundgren, C. A.; Xu, K.; Wang, Y.; Wang, C. Architecturing Hierarchical Function Layers on Self-Assembled Viral Templates as 3D Nano-Array Electrodes for Integrated Li-Ion Microbatteries. *Nano Lett.* **2013**, *13*, 293–300.
34. Royston, E.; Ghosh, A.; Kofinas, P.; Harris, M. T.; Culver, J. N. Self-Assembly of Virus-Structured High Surface Area Nanomaterials and Their Application as Battery Electrodes. *Langmuir* **2008**, *24*, 906–912.
35. Lee, S.; Royston, E.; Culver, J. M.; Harris, M. T. Improved Metal Cluster Deposition on a Genetically Engineered Tobacco Mosaic Virus Template. *Nanotechnology* **2005**, *16*, S435–S441.
36. Chen, X.; Gerasopoulos, K.; Guo, J.; Brown, A.; Wang, C.; Ghodssi, G.; Culver, J. N. Virus-Enabled Silicon Anode for Lithium-Ion Batteries. *ACS Nano* **2010**, *4*, 5366–5372.
37. Cui, L.-F.; Ruffo, R.; Chan, C. K.; Peng, H.; Cui, Y. Crystalline-Amorphous Core-Shell Silicon Nanowires for High Capacity and High Current Battery Electrodes. *Nano Lett.* **2009**, *9*, 491–495.
38. Bruce, P. G.; Scrosati, B.; Tarascon, J.-M. Nanomaterials for Rechargeable Lithium Batteries. *Angew. Chem., Int. Ed.* **2008**, *47*, 2930–2946.
39. Mukaiboa, H.; Mommaa, T.; Osaka, T. Changes of Electro-Deposited Sn-Ni Alloy Thin Film for Lithium Ion Battery Anodes During Charge Discharge Cycling. *J. Power Sources* **2005**, *146*, 457–463.
40. Nishikawa, K.; Fukunaka, Y.; Sakka, T.; Ogata, Y.; Selman, J. R. *In Situ* Measurement of Lithium Mass Transfer During Charging and Discharging of A Ni−Sn Alloy Electrode. *J. Power Sources* **2007**, *174*, 668–672.
41. Guo, H.; Zhao, H.; Jia, X. Spherical Sn-Ni-C Alloy Anode Material with Submicro/Micro Complex Particle Structure for Lithium Secondary Batteries. *Electrochem. Commun.* **2007**, *9*, 2207–2211.
42. Ehinon, K. K. D.; Naille, S.; Dedryvère, R.; Lippens, P.-E.; Jumas, J.-C.; Gonbeau, D. Ni_3Sn_4 Electrodes for Li-Ion Batteries: Li-Sn Alloying Process and Electrode/Electrolyte Interface Phenomena. *Chem. Mater.* **2008**, *20*, 5388–5398.
43. Nishikawa, K.; Dokkob, K.; Kinoshita, K.; Woo, S.-W.; Kanamura, K. Three-Dimensionally Ordered Macroporous Ni-Sn Anode for Lithium Batteries. *J. Power Sources* **2009**, *189*, 726–729.
44. Huang, L.; Wei, H.-B.; Ke, F.-S.; Fan, X.-Y.; Li, J.-T.; Sun, S.-G. Electrodeposition and Lithium Storage Performance of Three-Dimensional Porous Reticular Sn-Ni Alloy Electrodes. *Electrochim. Acta* **2009**, *54*, 2693–2698.
45. Woo, S.-W.; Okada, N.; Kotobuki, M.; Sasajima, K.; Munakata, H.; Kajihara, K.; Kanamura, K. Highly Patterned Cylindrical Ni-Sn Alloys with 3-Dimensionally Ordered Macroporous Structure as Anodes for Lithium Batteries. *Electrochim. Acta* **2010**, *55*, 8030–8035.
46. Noh, M.; Kwon, Y.; Lee, H.; Cho, J.; Kim, Y.; Kim, M. G. Amorphous Carbon-Coated Tin Anode Material for Lithium Secondary Battery. *Chem. Mater.* **2005**, *17*, 1926–1929.
47. Yu, Y.; Gu, L.; Wang, C.; Dhanabalan, A.; Aken, P. A. V.; Maier, J. Encapsulation of Sn@Carbon Nanoparticles in Bamboo-Like Hollow Carbon Nanofibers as An Anode Material in Lithium-Based Batteries. *Angew. Chem., Int. Ed.* **2009**, *48*, 6485–6489.
48. Derrien, G.; Hassoun, J.; Panero, S.; Scrosati, B. Nanostructured Sn-C Composite as an Advanced Anode Material in High-Performance Lithium-Ion Batteries. *Adv. Mater.* **2007**, *19*, 2336–2340.
49. Fan, J.; Wang, T.; Yu, C.; Tu, B.; Jiang, Z.; Zhao, D. Ordered, Nanostructured Tin-Based Oxides/Carbon Composite as the Negative-Electrode Material for Lithium-Ion Batteries. *Adv. Mater.* **2004**, *16*, 1432–1436.
50. Lee, K. T.; Jung, Y. S.; Oh, S. M. Synthesis of Tin-Encapsulated Spherical Hollow Carbon for Anode Material in Lithium Secondary Batteries. *J. Am. Chem. Soc.* **2003**, *125*, 5652–5653.
51. Kim, C.; Park, S.-H; Cho, J.-I; Lee, D.-Y; Park, T.-J; Lee, W.-J.; Yang, K.-S. Raman Spectroscopic Evaluation of Polyacrylonitrile-Based Carbon Nanofibers Prepared by Electrospinning. *J. Raman Spectrosc.* **2004**, *35*, 928–933.
52. Taberna, P. L.; Mitra, S.; Poizot, P.; Simon, P.; Tarascon, J.-M. High Rate Capabilities Fe_3O_4-Based Cu Nano-Architectured Electrodes for Lithium-Ion Battery Applications. *Nat. Mater.* **2006**, *5*, 567–573.
53. Shaijumon, M. M.; Perre, E.; Daffos, B.; Taberna, P.-L.; Tarascon, J, -M.; Simon, P. Nanoarchitectured 3D Cathodes for Li-Ion Microbatteries. *Adv. Mater.* **2010**, *22*, 4978–4981.
54. Wang, W.; Tian, M.; Abdulagatov, A.; George, S, M; Lee, Y.-C.; Yang, R. Three-Dimensional Ni/TiO_2 Nanowire Network for High Areal Capacity Lithium Ion Microbattery Applications. *Nano Lett.* **2012**, *12*, 655–660.